24th INTERNATIONAL CONGRESS ON SOUND AND VIBRATION
23–27 July 2017, London

ICSV24
23-27JULY 2017
LONDON CALLING

EXPERIMENTAL TESTS OF A FLYWHEEL INERTIAL ACTUATOR

Aleksander Kras and Paolo Gardonio

Università degli Studi di Udine, DPIA, Via delle Scienze 206, Udine, Italy
email: aleksander.kras@uniud.it

This paper presents the results of experimental tests carried out on a new inertial actuator that can be used to implement a velocity feedback loop to reduce the flexural vibration of flexible structures. Classical inertial actuators used in vibration control systems incorporate coil-magnet linear motors, with the magnet suspended on soft springs and the coil attached to the base. With this configuration there are two aspects that limit the effectiveness of the feedback vibration control system. Firstly, the inherent dynamics of the springs-magnet system limits the stability, and thus control performance of the feedback loop. Secondly, when exposed to shocks, the actuator suffers undesired stroke saturation effects, which may also lead to instability of the feedback loop. The inertial actuator presented in this paper includes an additional flywheel element that increases the inertia of the proof mass without increasing the weight of the suspended mass. As a result, the fundamental natural frequency of the actuator could be lowered without increasing the static displacement of the suspended mass. This improves the stability of the feedback loop, both by increasing the feedback gain margin and by improving the robustness to shocks. This paper presents the measured frequency responses functions that characterise the electro-mechanical response of a flywheel actuator prototype, which are contrasted with simulations obtained from a simplified lumped parameter model. The experimental results agree well with the simulation results and confirm that the new flywheel actuator can be effectively used to implement a more robust velocity feedback loop.
Keywords: Inerter, proof mass actuator, vibration control

1. Introduction

This paper presents the experimental tests carried out on a new inertial actuator equipped with a flywheel element, which was introduced in Refs. [1-3] for the implementation of more robust decentralised velocity feedback loops for vibration control of flexible structures. The electromechanical parameters of the tested flywheel inertial actuator are contrasted with simulation results obtained from a simplified mathematical model (see Refs. [1,3]) and compared with those of classical inertial actuators.

Elliott et al. [4], showed that flexural vibration of distributed two-dimensional thin structures can be effectively diminished with decentralised feedback systems using collocated point force actuator and velocity sensor pairs, which produce the so-called sky-hook damping effect [5]. As discussed in Refs. [6-14], a point force excitation can be obtained from inertial (also called proof mass) actuator, which is composed by a mass suspended on a spring with in parallel an electromechanical transducer. Normally, a coil–magnet transducer is used, which can withstand the large stroke necessary to produce the desired levels of control force [14]. However, the internal dynamics of the inertial actuator, i.e. its resonant response, makes the feedback control loop only conditionally stable [12]. In general, to mitigate this problem, the inertial actuator should be designed with a very low fundamental resonance frequency. However, this solution tends to enhance the static displacement of the proof mass and this could lead to stroke saturation effects, which may also cause instability problems [10,15-18].

All these stability issues become even more severe when multiple feedback loops are implemented [19-21]. Therefore, several approaches have been investigated over the years to alleviate these problems. For example the implementation of internal displacement, velocity and force feedback loops have been studied to minimise the stroke at the fundamental resonance of proof mass actuators [22-24]. Alternatively various types of feedback controllers have been considered, which, in general, also aim to compensate the second order dynamics of the proof mass actuator [25-30].

This paper considers the implementation of a new proof mass actuator with a flywheel element [1-3], which resembles the mechanical element called "inerter" [31,32]. The flywheel produces an apparent mass effect that increases the inertia of the suspended mass, though without increasing its weight and thus without degrading the static displacement properties of the actuator. Therefore the new actuator can be designed with relatively low fundamental resonance frequency and with rather low static displacement, so that it can be effectively used to implement stable and robust point velocity feedback loops.

This paper presents the initial tests carried out on a classical coil-magnet proof mass actuator that can be equipped with a rocker arm having movable lumped masses, whose dynamic effect resemble that of a flywheel element. The paper is organised in five sections. Section two describes the details of the rig built for this study. Section three briefly recalls the analytical formulation used to derive the measured response functions. Section four contrasts the simulated and measured frequency response functions (FRFs) for a) the base impedance, b) the blocked force per unit input current and c) the electrical impedance that characterise the classical and newly proposed proof mass actuators.

2. Flywheel inertial actuator

Normally inertial actuators for active vibration control are based on linear electromagnetic motor. In this study the transducer shown in Fig. 1a is used as reference actuator. As depicted schematically in Fig. 1c, this actuator is formed by a magnetic inner cylinder, which is attached to the structure and acts as a base mass m_b. Instead, the external coil armature cylinder acts as a proof mass M_a, which is suspended to the inner element via two flexural springs of stiffness k and damping c. The electromagnetic effect of the actuator is modelled in terms of transduction coefficient ψ_a that produces a pair of forces F_a proportional to the current i_a flowing in coil, which is characterised by resistance R and inductance L effects. The same transduction coefficient produces the back electromotive force u_{em} that is proportional to the relative velocity $\dot{w}_m - \dot{w}_b$ between the proof mass (coil) and the case (magnet) of the actuator.

As shown in Fig. 1b, the same electromagnetic actuator is then equipped with a rocker arm having lumped masses at the ends, which produces the desired rotational inertial effect proportional to the relative axial motion between the inner cylindrical magnet and exterior armature coil element. This actuator is thus characterised by an additional relative inertia effect, which, as depicted schematically in Fig. 1d, is modelled with an inerter element [31] connected in parallel with the suspension spring and damper elements. This element is characterised by a mass m_w, which adds to the proof mass M_a, and by a polar moment of inertia I_w. The relative motion between the inner and outer cylindrical elements of the actuator was converted into a rotation of the rocker arm by hinging the arm to a post connected to the inner cylindrical magnet and to a bracket fixed to the external armature-coil element. The bracket was designed with four hinging points, so that the conversion offset r_w from axial to rotational motion could be changed. In this way, the resulting equivalent relative axial inertia effect of the rocking arm I_w/r_w^2 was varied. The hinges produce a rotational damping effect c_w, which is also converted into axial damping given by c_w/r_w^2. The physical properties of the coil-magnet actuator and rocker arm element are summarised in Table 1. The table specifies the equivalent axial inertia effects of the rocker arm element with reference to the four hinging positions, i.e. with reference to the four offsets r_w.

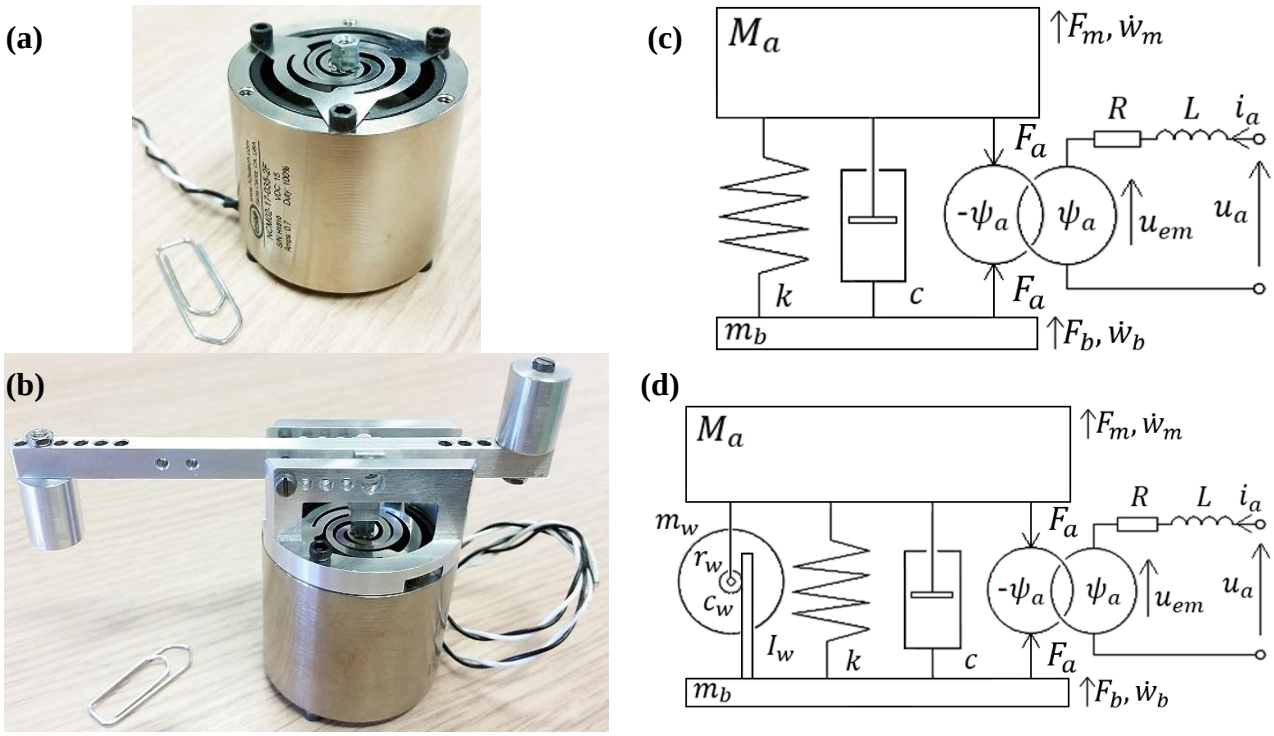

Figure 1: Pictures (a,b) and schemes (c,d) of the tested classical (a,c) and the flywheel inertial actuator (b,d).

Table 1: Mechanical parameters of the inertial actuators

Parameter	Value
Proof mass / Coil mass	$M_a = 0.203$ kg
Case mass / Magnet mass	$m_b = 0.117$ kg
Flywheel mass	$m_w = 0.03$ kg
Axial stiffness	$k = 2950\ \mathrm{Nm}^{-1}$
Damping ratio	$\zeta = 0.2$
Flywheel polar moment of inertia	$I_p = 6.47 \cdot 10^{-5}\ \mathrm{kgm}^2$
Torsional damping ratio	$\zeta_w = 0.005$
Flywheel inertia values	$I_{w1} = 7.4;\ I_{w2} = 7.0;\ I_{w3} = 6.7;\ I_{w4} = 6.5 \cdot 10^{-5}\ \mathrm{kgm}^2$
Pushing pin offset values	$r_{w1} = 17\ ; r_{w2} = 13\ ; r_{w3} = 9\ ;\ r_{w4} = 5$ mm
Axial mass effect of the flywheel	$\frac{I_{w1}}{r_{w1}^2} = 0.26;\ \frac{I_{w2}}{r_{w2}^2} = 0.42;\ \frac{I_{w3}}{r_{w3}^2} = 0.83;\ \frac{I_{w4}}{r_{w4}^2} = 2.62$ kg
Coil resistance	$R = 23.5\ \Omega$
Coil inductance	$L = 4.35 \cdot 10^{-3}\mathrm{H}$
Transduction coefficient	$\psi_a = 22.5\ \mathrm{NA}^{-1}$

3. Actuators mathematical models

This section briefly recall the mathematical formulation used to derive the frequency response functions (FRF) for the base impedance, electrical impedance and blocked force per unit input current that characterise the electromechanical response of the classical (Figs. 1a,c) and flywheel (Figs. 1b,d) proof mass actuators. The details of the mathematical formulations can be found in Ref. [3]. The frequency domain formulation is derived with reference to the complex amplitudes $g(\omega)$ of time–harmonic functions given in the form $g(t) = \mathrm{Re}\{g(\omega)\exp(\mathrm{j}\omega t)\}$, where ω is the circular frequency and $\mathrm{j}^2 = -1$. For simplicity, the frequency dependence is omitted in the expressions of the FRFs.

Considering the lumped parameter models shown in Figs. 1c,d, the base impedance, the blocked force per unit driving current and the electrical impedance of the actuators are given by:

$$Z_{f\dot{w}} = \frac{-F_b}{\dot{w}_b}\bigg|_{i_a=0} = Z_b + \frac{Z_a}{1+Y_m Z_a}\,. \tag{1}$$

$$F_{fi} = \frac{F_b}{i_a}\bigg|_{\dot{w}_b=0} = \frac{\psi_a}{1+Y_m Z_a}\,. \tag{2}$$

$$Z_{ui} = \frac{u_a}{i_a}\bigg|_{\dot{w}_b=0} = Z_e + \frac{Y_m \psi_a^2}{1+Y_m Z_a}\,. \tag{3}$$

In these equations Z_a and Y_m depend on the type of the actuator and for the classical actuator are defined as $Z_a = c + \frac{k}{\mathrm{j}\omega}$ and $Y_m = \frac{1}{\mathrm{j}\omega M_a}$, while for the flywheel actuator are defined as $Z_\mathrm{a} = c + \frac{k}{\mathrm{j}\omega} + \mathrm{j}\omega\frac{I_w}{r_w^2} + \frac{c_w}{r_w^2}$ and $Y_m = \frac{1}{\mathrm{j}\omega(M_a+m_w)}$, where the damping is defined as $c = \zeta 2\sqrt{M_a k}$ for the classical actuator and $c = \zeta 2\sqrt{(M_a + I_w/r_w^2 + m_w)k}$ for the flywheel actuator. The impedance of the actuator base mass is given by $Z_b = \mathrm{j}\omega m_b$. Finally $Z_e = \mathrm{j}\omega L + R$.

4. Experimental tests

The following subsections contrasts the measured and simulated base impedance, blocked force per unit input current and electrical impedance of the classical and flywheel proof mass actuators. The FRFs are depicted in a 5×2 matrix of plots. The left hand side plots show the moduli while the right hand side plots show the phase of the measured (solid blue lines) and simulated (dash-dotted red lines). The plots in the first row shows the FRFs for the reference actuator without flywheel while the plots in the other four rows shows the FRFs for the reference actuator with the rocker arm hinged with a progressively smaller offset ($r_{w1} > r_{w2} > r_{w3} > r_{w4}$) such that the equivalent relative axial inertia effect of the flywheel is progressively increased ($\frac{I_{w1}}{r_{w1}^2} < \frac{I_{w2}}{r_{w2}^2} < \frac{I_{w3}}{r_{w3}^2} < \frac{I_{w4}}{r_{w4}^2}$).

4.1 Base impedance

The first row of plots in Fig. 2a show the typical modulus and phase diagrams that characterise the base impedance of a proof mass actuator [33], which is characterised by low and high frequencies asymptotic mass behaviours, proportional respectively to the total mass $M_a + m_b$ and the case mass m_b of the actuator. The two asymptotes are separated by a resonance peak and an antiresonance through respectively at about the fundamental resonance frequency of 20 Hz and at about 32 Hz. The remaining four rows of plots in Fig. 2b-e show the effects produced by the rocker arm hinged with a progressively smaller offset such that its equivalent relative axial inertia effect I_w/r_w^2 is progressively increased. The fundamental resonance frequency moves progressively to lower frequencies; that is to about 12 Hz (Fig. 2b), to about 10 Hz (Fig. 2c), to about 8.5 Hz (Fig. 2d) and to about 6.5 Hz (Fig. 2e). Also, the amplitude of the higher frequency asymptotic mass behaviours is progressively increased. Finally the internal damping effect in the proof mass actuator is also increased, such that the resonance peak and antiresonance through are progressively rounded. The simulated impedance FRFs align reasonably well with the experimental results for all configurations except the last one. For the highest value of equivalent relative axial inertia effect I_{w4}/r_{w4}^2 (Fig. 2e) the simulation result gives lower actuator resonance frequency compared to the experiment. Furthermore, the high relative axial inertia effect introduces additional dynamics to the system that result in a wide band crest followed by a wide band between 50 and 100 Hz. The impedance measured on the classical actuator shown in Fig. 2a is characterised by a glance at about 39 Hz, which is not predicted in the simulation. It is likely that this peak is linked to a resonant rocking mode of the suspended mass, which is however removed when the rocker arm is fixed to the actuator.

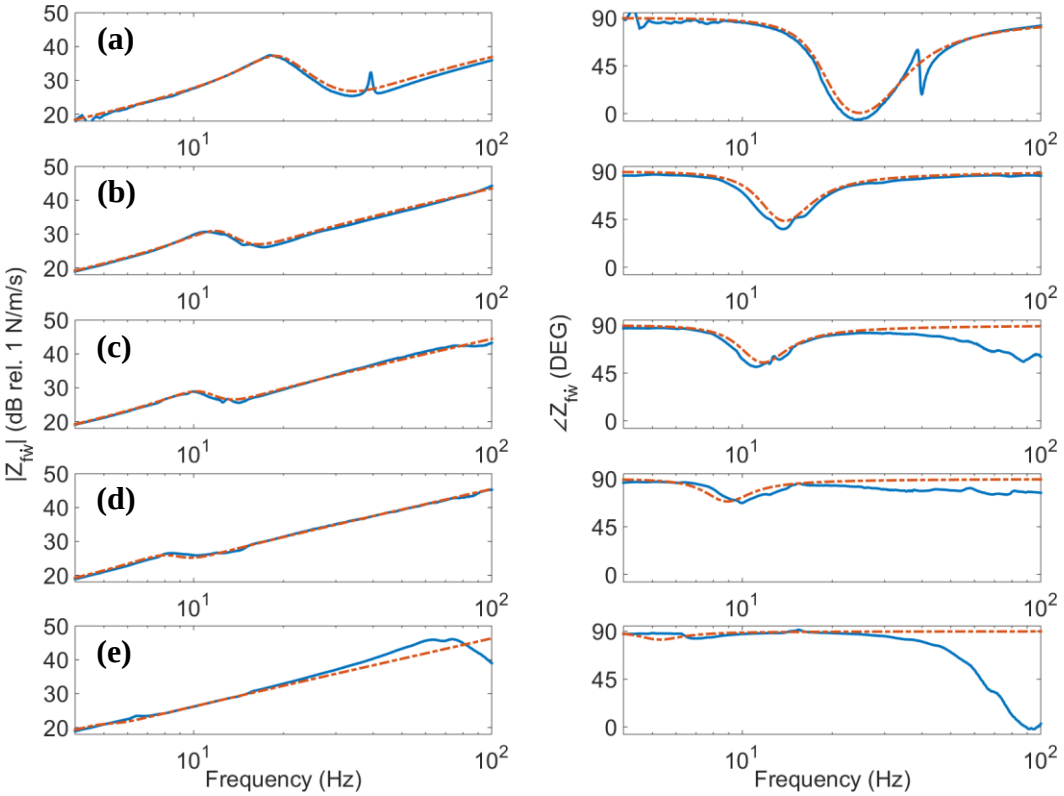

Figure 2: Base impedance for the reference actuator (a) and for the flywheel actuator with inertia $\boldsymbol{I_{w1}}$ (b), inertia $\boldsymbol{I_{w2}}$ (c), inertia $\boldsymbol{I_{w3}}$ (d) and inertia $\boldsymbol{I_{w4}}$ (e). Experimental results (solid blue lines). Simulations (dashed-dotted red lines).

4.2 Blocked force

The first row of plots in Fig. 3a show the typical modulus and phase diagrams that characterise the blocked force per unit driving current of a proof mass actuator [33]. At low frequency the force rises proportionally to ω^2 and is out of phase with the driving current signal. The force peaks at the fundamental resonance frequency of the proof mass actuator, i.e. about 20 Hz, and then rapidly decreases and settle to a constant value equal to the transduction coefficient, i.e. 27dB, in phase with the driving current. Thus the proof mass actuator produces the desired constant force excitation in phase with the driving signal at frequencies above its fundamental resonance frequency. At lower frequencies the force produced is out of phase with the driving signal. Thus when this actuator is used to implement a negative velocity feedback to mimic a sky-hook damper, at frequencies below the fundamental resonance frequency, the feedback loop essentially produces a positive velocity feedback effect, that is a negative damping effect, which could lead to instability. It is therefore vitally important the fundamental resonance frequency is as low as possible and the amplitude of the resonance peak is also the minimum possible. The remaining four rows of plots in Fig. 3b-e show that when the actuator is equipped with the rocker arm hinged with an increasingly smaller offset and thus the equivalent relative axial inertia effect of the rocking arm I_w/r_w^2 is progressively increased, the resonance peak is progressively smoothened and brought down in frequency. Also, the higher frequencies constant force excitation is also progressively lowered to about 21 dB, 18 dB, 14 dB, 6 dB. Also the simulated force per unit driving current FRFs agree reasonably well with the experimental results. As seen above, the classical actuator is characterised by a rocking effect of the proof mass, which produces a small peak at about 39 Hz. Also, at frequencies above fundamental resonance frequency of the actuator, the rocker arm brings in additional dynamic effects, which results in additional small peaks at about 50 Hz and around 100 Hz (particularly for the configuration with the smallest offset).

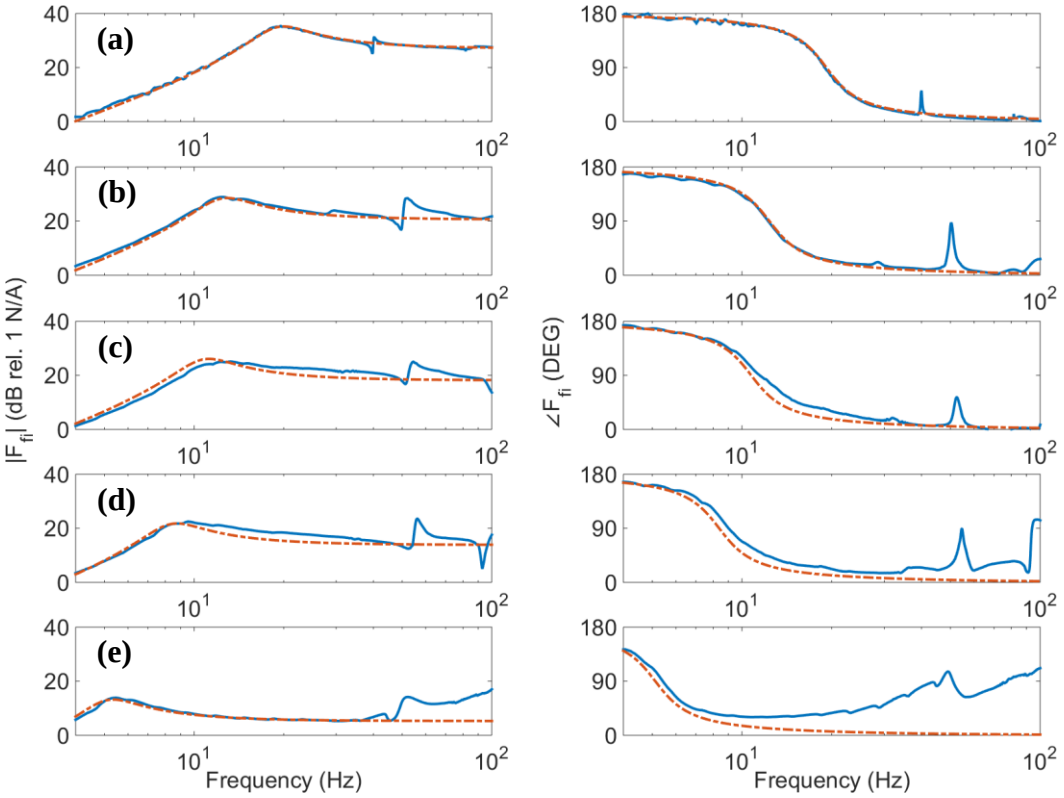

Figure 3: Blocked force for the reference actuator (a) and for the flywheel actuator with inertia $\boldsymbol{I_{w1}}$ (b), inertia $\boldsymbol{I_{w2}}$ (c), inertia $\boldsymbol{I_{w3}}$ (d) and inertia $\boldsymbol{I_{w4}}$ (e). Experimental results (solid blue lines). Simulations (dashed-dotted red lines).

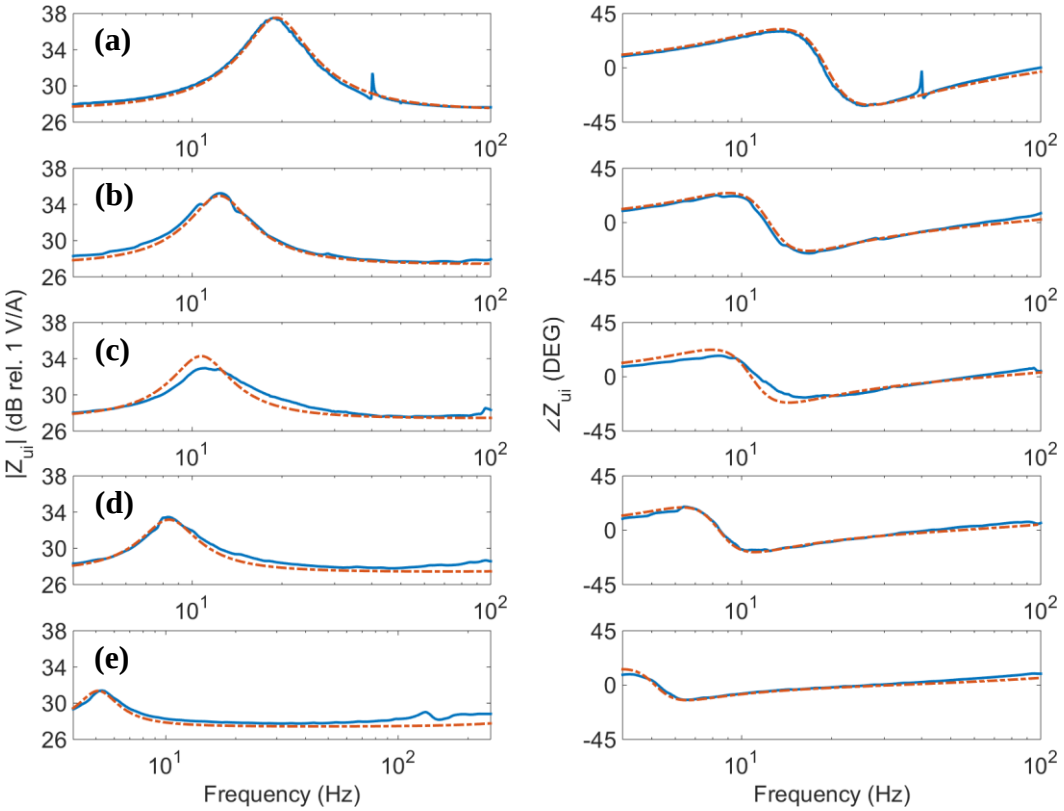

Figure 4: Electrical impedance for the reference actuator (a) and for the flywheel actuator with inertia $\boldsymbol{I_{w1}}$ (b), inertia $\boldsymbol{I_{w2}}$ (c), inertia $\boldsymbol{I_{w3}}$ (d) and inertia $\boldsymbol{I_{w4}}$ (e). Experimental results (solid blue lines). Simulations (dashed-dotted red lines).

4.3 Electrical impedance

The first row of plots in Fig. 4a show the typical modulus and phase diagrams that characterise the electrical impedance FRF of a coil-magnet proof mass actuator, which is given by the superposition of the of the coil Z_e and the electro-mechanical effect $\frac{Y_m \psi_a^2}{1+Y_m Z_a}$. In the 0 – 100 Hz frequency range, the coil electrical impedance is purely resistive. Also, the electro-mechanical effect is relevant only around the fundamental resonance frequency of the actuator. Thus the spectrum is characterised by a constant value of about 27.5 dB and phase zero for the resistive component and, around at about 20 Hz, a resonance peak and a phase swing to about ±30°, which is due to the electro-mechanical effect of the proof mass actuator. The remaining four rows of plots in Fig. 4b-e show that when the actuator is equipped with the rocker arm hinged with an increasingly smaller offset and thus the equivalent relative axial inertia effect of the rocking arm I_w/r_w^2 is progressively increased, the resonance peak is progressively smoothened and brought down in frequency. The simulated impedance FRFs agree quite well with the measured FRFs, particularly because the higher dynamic effects introduced by the rocker arm element occur at higher frequencies than the fundamental resonance frequency of the proof mass actuator and thus are not rendered into the electrical impedance.

5. Conclusions

This paper has presented experimental and simulation results on the FRFs that characterise the electromechanical response of a new flywheel inertial actuator, which can be used to implement a velocity feedback loop to reduce the flexural vibration of flexible structures. The study has considered the mechanical base impedance, the blocked force per input current and the electrical impedance FRFs. The measured FRFs were taken on a classical coil-magnet inertial actuator equipped with a rocker arm system specifically designed to produce a variable flywheel inertia effect. The simulated FRFs were derived from a lumped parameter model.

The study has shown reasonably good agreement between the measured and simulated FRFs. Also, it has confirmed that the rotational inertia effect of the flywheel element tends to reduce the resonance frequency and the amplitude of the fundamental resonance peak that characterise the response of the actuator without increasing the static deflection of the actuator. Thus the new flywheel inertial actuator could be used to implement more stable and robust velocity feedback loops to control the vibration of mechanical systems and flexible structures.

Acknowledgments

The authors gratefully acknowledge the European Commission for its support of the Marie Skłodowska-Curie program through the ITN ANTARES project (GA 606817).

REFERENCES

1 Kras, A. and Gardonio, P. Flywheel proof mass actuator for velocity feedback control, *Proceedings of the MoViC–RASD 2016 International Conference on Recent Advances in Structural Dynamics*, Southampton, UK, 3-6 July, (2016).

2 Kras, A. and Gardonio, P. Flywheel inertial actuator for velocity feedback control: parametric study, *Proceedings of the ISMA2016 International Conference on Noise and Vibration Engineering*, Leuven, Belgium, 19-21 September, (2016).

3 Kras, A. and Gardonio, P. Velocity feedback control with a flywheel proof mass actuator, *Journal of Sound and Vibration*, (2017).

4 Elliott, S. J., Gardonio, P., Sors, T. J. and Brennan, M. J. Active vibroacoustic control with multiple local feedback loops. *The Journal of the Acoustical Society of America*, **111** (2), 908-915, (2002).

5 Balas, M. Direct velocity feedback control of large space structures, *Journal of Guidance, Control, and Dynamics*, **2** (3), 252–253, (1979).

6 Miller, D. W. and Crawley, E. F. Theoretical and experimental investigation of space-realizable inertial actuation for passive and active structural control, *Journal of Guidance, Control, and Dynamics*, **11** (5), 449–458, (1988).

7 Zimmerman, D. C., Hornar, G. C. and Inman, D. J. Microprocessor Controlled Force Actuator, *Journal Guidance, Control, and Dynamics*, **11** (3), 230-236, (1988).
8 Politansky, H. and Pilkey, W. D. Suboptimal feedback vibration control of a beam with a proof-mass actuators, *Journal of Guidance, Control, and Dynamics* **12** (5), 691–697, (1989).
9 Zimmerman, D. C. and Inman, D. J. On the nature of the interaction between structures and proof-mass actuators, *Journal of Guidance, Control, and Dynamics*, **13** (1), 82–88, (1990).
10 Lindner, D. K., Celano, T.P. and Ide, E. N. Vibration suppression using a proof mass actuator operating in stroke/force saturation, *Journal of Vibration and Acoustics*, **113** (4), 423–433, (1991).
11 Garcia, E., Webb, S. and Duke, J. Passive and active control of a complex flexible structure using reaction mass actuators, *Journal of Vibration and Acoustics Transactions of the ASME*, **117** (1), 116–122, (1995).
12 Elliott, S. J., Serrand, M. and Gardonio, P. Feedback stability limits for active isolation systems with reactive and inertial actuators, Journal of Vibration and Acoustics, **123** (2), 250–261, (2001).
13 Griffin, S., Gussy, J., Lane, S. A., Henderson, B. K. and Sciulli, D. Virtual skyhook vibration isolation system, *Journal of Vibration and Acoustics*, **124** (1), 63–67, (2001).
14 Gonzalez Diaz, C., Paulitsch, C. and Gardonio, P. Active damping control unit using a small scale proof mass electrodynamic actuator, *Journal of the Acoustical Society of America*, **124** (2), 886-897, (2008).
15 Lindner, D., Zvonar, G. and Borojevic, D. Performance and control of proof-mass actuators accounting for stroke saturation, *Journal of Guidance, Control, and Dynamics*, **17** (5), 1103–1108, (1994).
16 Chase, J. G., Yim, M. and Berlin, A. A. Integrated centering control of inertially actuated systems, *Control Engineering Practice*, **7** (9), 1079-1084, (1999).
17 Baumann, O. N. and Elliott, S. J. Destabilization of velocity feedback controllers with stroke limited inertial actuators, *The Journal of the Acoustical Society of America*, **121** (5), 211–217, (2007).
18 Dal Borgo, M. Ghandchi Tehrani, M. and Elliott, S. J. Dynamic analysis of nonlinear behaviour in inertial actuators, *Journal of Physics: Conference Series*, **744** (1), 1-12, (2016)
19 Baumann, O. N. and Elliott, S. J. The stability of decentralized multichannel velocity feedback controllers using inertial actuators, *Journal of the Acoustical Society of America*, **121** (1), 188–196, (2007).
20 Gonzalez Diaz, C., Paulitsch, C. and Gardonio, P. Smart panel with active damping units. Implementation of decentralized control, *Journal of the Acoustical Society of America*, **124** (2), 898-910, (2008).
21 Rohlfing, J., Gardonio, P. and Thompson, D. J. Comparison of decentralized velocity feedback control for thin homogeneous and stiff sandwich panels using electrodynamic proof-mass actuators, *Journal of Sound and Vibration*, **330**, 843–867, (2011).
22 Benassi, L. and Elliott, S. J. Active vibration isolation using an inertial actuator with local displacement feedback control, *Journal of Sound and Vibration*, **278** (4–5), 705–724, (2004).
23 Paulitsch, C., Gardonio, P. and Elliott, S. J. Active vibration control using an inertial actuator with internal damping, *Journal of the Acoustical Society of America*, **119** (4), 2131–2140, (2006).
24 Benassi, L., Elliott, S. J. and Gardonio, P. Active vibration isolation using an inertial actuator with local force feedback control, *Journal of Sound and Vibration*, **276** (1-2), 157-179, (2004).
25 Gonzalez Diaz, C. and Gardonio, P. Feedback control laws for proof-mass electro-dynamic actuators, *Journal of Smart Materials and Structures*, **16**, 1766-1783, (2007).
26 Lanzon, A. and Petersen, I. R. Stability robustness of a feedback interconnection of systems with negative imaginary frequency response, *IEEE Transactions on Automatic Control*, **53**, 1042–1046, (2008).
27 Diaz, I. M. and Reynolds, P. Acceleration feedback control of human-induced floor vibrations, *Engineering Structures*, **32** (1), 163-173, (2010).
28 Diaz, I. M., Pereira, E. and Reynolds, P. Integral resonant control scheme for cancelling human-induced vibrations in light-weight pedestrian structures, *Structural Control and Health Monitoring*, **19** (1), 55–69, (2011).
29 Pereira, E., Aphale, S. S., Feliu, V. and Moheimani, S. O. R. Integral resonant control for vibration damping and precise tip-positioning of a single-link flexible manipulator, *IEEE/ASME Transactions on Mechatronics*, **16** (2), 232-240, (2011).
30 Rohlfing, J., Elliott, S. J. and Gardonio, P. Feedback compensator for control units with proof-mass electrodynamic actuators, *Journal of Sound and Vibration*, **331** (15), 3437–3450, (2012).
31 Smith, M., Synthesis of mechanical Networks: The Inerter, *IEEE Transactions on automatic control*, **47**, 1648–1662, (2002).
32 Zilletti, M., Feedback control unit with an inerter proof-mass electrodynamic actuator, *Journal of Sound and Vibration*, **369**, 16–28, (2016).
33 Rohlfing, J., Gardonio, P. and Elliott, S. J. Base impedance of velocity feedback control units with proof-mass electrodynamic actuators, *Journal of Sound and Vibration*, **330** (20), 4661-4675, (2011).